ACS APPLIED MATERIALS & INTERFACES

www.acsami.org

Research Article

Wavelength-Tunable Optical Fiber Localized Surface Plasmon Resonance Biosensor *via* a Diblock Copolymer-Templated Nanorod Monolayer

Mengdi Lu, Hu Zhu, Long Hong, Jijun Zhao, Jean-Francois Masson,* and Wei Peng*

Cite This: https://dx.doi.org/10.1021/acsami.0c09711

Read Online

ABSTRACT: Well-dispersed and dense layers of gold nanorods (AuNRs) on optical fibers are shown to regulate the longitudinal peak wavelength and enhance the sensing performances of localized surface plasmon resonance (LSPR) biosensors. A simple self-assembly method relying on a brush-like monolayer of poly(styrene)-*b*-poly(acrylic acid) (PS-*b*-PAA) diblock copolymer was used to immobilize AuNRs with various aspect ratios from 2.33 to 4.60 on optical fibers. Both the experimental and simulation results illustrated that the particle aspect ratio, deposition time (related to the coverage of AuNRs), and interparticle gap significantly affected the optical properties of the fiber-based LSPR biosensors. The highest refractive index (RI) sensitivity of the sensor was 753 nm/RIU, while the limit of detection for human IgG was as low as 0.8 nM. Compared with standard nanoparticle deposition methods of polyelectrolytes or alkoxysilanes, the RI sensitivity of the PS-*b*-PAA dip-coating method was approximately 3-fold better, a consequence of the higher particle coverage and fewer AuNR aggregates. The presented AuNR-based LSPR sensors could regulate the detection range by tuning the aspect ratios of AuNRs. Applicability is demonstrated *via* quantitative analysis of antigen−antibody interactions, DNA sensing, and surface-enhanced Raman scattering.

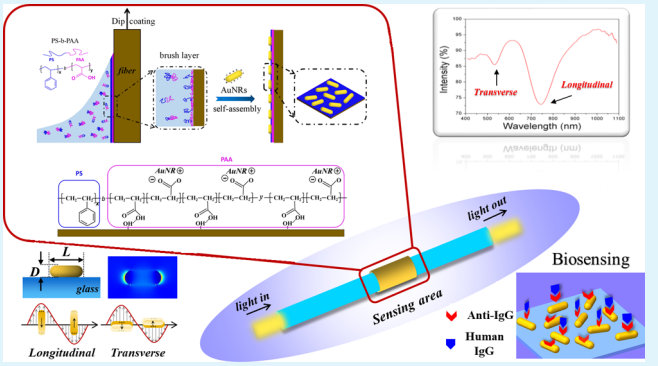

KEYWORDS: *fiber optics, localized surface plasmon resonance, biosensor, gold nanorod, diblock copolymer*

INTRODUCTION

Plasmonic metallic nanoparticles strongly absorb and scatter light because of localized surface plasmon resonance[1] (LSPR). The dependence of the resonance condition on the local dielectric environment enables a simple form of molecular sensing[2,3] in which analyte binding to the nanoparticle surface causes a red shift in the spectral absorption peak,[4] which allows applications of plasmonic nanoparticles as LSPR sensors for real-time biochemical analysis.[5−7] An LSPR sensor is therefore the nanoparticle analog of an SPR sensor,[8] which similarly monitors the resonance condition of surface plasmons in thin metal films.[9]lthough SPR is a powerful analytical technique for monitoring biomolecular interactions[10] and used as a screening tool for therapeutic and diagnostic applications,[11] it is still not commonly used in clinical immunoassays owing to the difficulty of working with complex biofluids[12] and complicated optical instruments and the precise temperature control requirements. Nonetheless, SPR sensors have been employed in a series of biomedical sensors.[13−16] LSPR sensors address some of the abovementioned technical challenges of SPR while retaining the advantages of SPR sensors.[17] One key feature is the greater applicability to clinical and medical applications, as the LSPR sensors are based on simpler optical absorption measurements and are nearly temperature-insensitive.[18]

In recent years, LSPR sensors based on various structures have been developed and reported and include solution phase,[19] chip-based,[20] and optical fiber[21,22] LSPR sensors. Note that optical fiber-based LSPR sensors have many advantages, including simplified optical design, low-cost, low sample volume requirements, resistance to electromagnetic (EM) interference, and remote sensing capability. Thereby, optical fiber-based LSPR sensors have been subject to intensive research, such as label-free biosensing to monitor heavy metal ions,[23,24] biotin-streptavidin,[25] and antigen−antibody interactions.[26−28] Furthermore, as the properties of metallic nanoparticles are highly dependent on their material, size,

Received: May 27, 2020
Accepted: October 19, 2020

and shape, controlling these parameters can optimize the LSPR sensing performance.[29]

Early on, the development of LSPR biosensors had mainly been focused on spherical gold nanoparticles[30] because of their ease of synthesis.[31] However, recent reports have shown that LSPR sensors based on noble metallic nanoparticles with various shapes have better optical performances[32] than gold nanosphere-based LSPR sensors. Among these metallic nanoparticles, gold nanorods (AuNRs) are favored because of their unique optical properties.[6,33,34] By manipulating the aspect ratio of AuNRs, the LSPR longitudinal peak wavelength can conveniently be regulated throughout the visible and near-infrared regions and into the infrared region,[35,36] allowing the LSPR sensor to be applied to particular applications where a specific wavelength and high refractive index (RI) sensitivity are desired.[37,38]

The fabrication of dense and well-dispersed AuNRs is crucial for the performance of LSPR sensors. Hexadecyltrimethylammonium bromide (CTAB) is the micellar surfactant commonly used in the batch synthesis of AuNRs,[36] but CTAB is cationic and moderately cytotoxic.[39,40] The preparation of CTAB-stabilized AuNR-based optical fiber LSPR sensors mainly relies on self-assembled monolayers (SAMs) of functionalized alkoxysilanes,[41] such as 3-mercaptopropyltrimethoxysilane (MPTMS), which is used as a linking agent *via* the S−Au covalent bond to assemble gold nanoparticles.[42] However, CTAB has proven to be notoriously difficult to replace because of not only its interactions with the gold surface but also hydrophobic interactions between adjacent hydrocarbon chains.[43] Oftentimes, this leads to the fabrication of surfaces with low nanoparticle coverage.[21]

To circumvent these issues, a polyelectrolyte method was presented to simplify the fabrication process.[44] A multilayer polyelectrolyte structure[45] with negative charges served as a linker to connect CTAB-stabilized AuNRs, which could greatly reduce the deposition time and enhance the RI sensitivity of the LSPR sensors compared with the alkoxysilane method. However, this polyelectrolyte method caused aggregation at higher particle coverage,[46] which is detrimental to the plasmonic properties of the LSPR sensor.[47] Moreover, the surface ligand exchange method could also contribute to the high density and well-dispersed AuNR SAMs, but complex preparation processes are required and may cause more particle aggregation.[48]

Asymmetric, amphiphilic diblock copolymers can self-assemble on substrates to form a thin monolayer in selective solvents, and then, AuNRs can be patterns on the self-assembled diblock copolymer-based monolayer.[49,50] As we recently reported,[17,51] the amphiphilic diblock copolymer poly(styrene-*b*-4-vinylpyridine) (PS-*b*-P4VP) could be used for the self-assembly of negatively charged gold nanospheres. However, the PS-*b*-P4VP monolayer cannot assemble the CTAB-stabilized AuNRs on the fiber as both of them are positively charged. Hence, we introduce a new surface chemistry using polystyrene-*b*-polyacrylic acid (PS-*b*-PAA) amphiphilic diblock copolymer for the assembly of AuNRs on substrates. PS-*b*-PAA has a hydrophobic PS block and a hydrophilic PAA block[52] and favors adsorption on glass substrates while also absorbing AuNRs through PAA chains, a weak polyelectrolyte.[53] We show that the optical fiber LSPR sensors can be coated with dense and well-dispersed AuNR monolayers for protein detection, with a significant gain in sensitivity and sensor performance compared to previous methods.

EXPERIMENTAL SECTION

Materials. Hydrogen tetrachloroaurate trihydrate ($HAuCl_4 \cdot 3H_2O$), sodium borohydride ($NaBH_4$, 99%), hexadecyltrimethylammonium bromide (CTAB, > 98.0%), silver nitrate ($AgNO_3$, >99%), sodium oleate (NaOL, > 97.0%), L-ascorbic acid (AA, >99%), MPTMS, 11-mercaptoundecanoic acid (11-MUA), 4-mercaptobenzoic acid (4-MBA), *N*-hydroxysuccinimide (NHS), 1-ethyl-3-(3-dimethylaminopropyl)carbodiimide hydrochloride (EDC), hydrochloric acid (HCl, 37 wt % in water), tetrahydrofuran (THF), and ethanol were obtained from Aladdin. Poly(4-styrenesulfonic acid) (PSS, 18 wt %, 65 kDa), poly-diallyldimethylammonium chloride (PDDA, 20 wt %, 150 kDa), and poly(allylamine) (PAH, 10 wt %, 65 kDa) were obtained from Sigma-Aldrich. Diblock copolymer polystyrene-*b*-polyacrylic acid (PS-*b*-PAA, $M_n \times 10^3$: 65-*b*-80, M_w/M_n: 1.09) was purchased from Polymer Source. Affinipure goat antihuman gamma globulin (H + L) (antihuman IgG), human gamma globulin (human IgG), bovine serum albumin, ssDNA strands, and phosphate buffer (phosphate-buffered saline (PBS), pH 7.4) were purchased from Sangon Biotech. Normal human serum was purchased from Scantibodies Laboratory. Ultrapure water (18 MΩ·cm) was used for all solutions.

Synthesis of AuNRs and Characterization. Gold nanorods with various aspect ratios from 2.3 to 4.6 were employed as the basis elements to functionalize the optical fiber LSPR biosensors and were prepared by following the methods of previous reports.[54,55] In brief, a two-stage protocol was developed to synthesize CTAB-stabilized AuNRs.

First, the seed solution was prepared as follows: fresh $NaBH_4$ (0.6 mL, 0.01 M, used within 2 min of its preparation) was diluted to prepare a 1 mL aqueous solution and then mixed with $HAuCl_4$ (0.5 mM, 5 mL) and CTAB (0.2 M, 5 mL) solutions under vigorous stirring for 5 min. The color of the solution changed from yellow to brownish yellow once $NaBH_4$ was injected. This seed solution was aged for 30 min at 30 °C before further use.

The growth solution was prepared at the same time with defined amounts of CTAB and additives (Table S1) dissolved in 100 mL of warm water (~70 °C). The solution was allowed to cool down and kept at 30 °C during the next process. Certain amounts of 4 mM $AgNO_3$ were mixed and left to stabilize for 15 min, after which 100 mL of 1 mM $HAuCl_4$ solutions followed. The solution became colorless after 150 min of slight stirring (700 rpm), and a certain volume of HCl, as detailed in Table S1, was then introduced with slow stirring (400 rpm) to adjust the pH. The solution was vigorously stirred for 30 s after 0.5 mL of 0.064 M ascorbic acid was added. Finally, a defined amount of seed solution was introduced under vigorous stirring for 30 s, and the resultant solution was left undisturbed at 30 °C for 12 h for AuNR growth. Prior to the immobilization of AuNRs on the fiber surface, the excess CTAB in particle solution was removed by centrifuging twice at 8000 rpm for 20 min each time, and no shape- or size-selective fractionation was performed.

The mean diameter and aspect ratio of the AuNRs were measured by transmission electron microscopy (TEM) (Tecnai G2F30, Thermo Scientific Inc.). The absorbance spectra of the AuNR solutions were obtained by a UV−vis spectrophotometer (Lambda 750S, PerkinElmer Inc.).

Fabrication of AuNRs on the Optical Fiber Surface. Plastic cladded silica multimode optical fibers were first cleaned and surface hydroxylated according to the methods we reported in previous work.[17]

For AuNR deposition, the processed fiber was immersed into a diblock copolymer (BCP) solution using a dip-coating method. The BCP solution (PS-*b*-PAA) was prepared at a concentration of 0.05 mg/mL by dilution in a THF solution obtained from a more concentrated solution (1 mg/mL). A brush-like BCP layer was obtained using a home-made dip-coater, and the fiber was vertically

https://dx.doi.org/10.1021/acsami.0c09711
ACS Appl. Mater. Interfaces XXXX, XXX, XXX−XXX

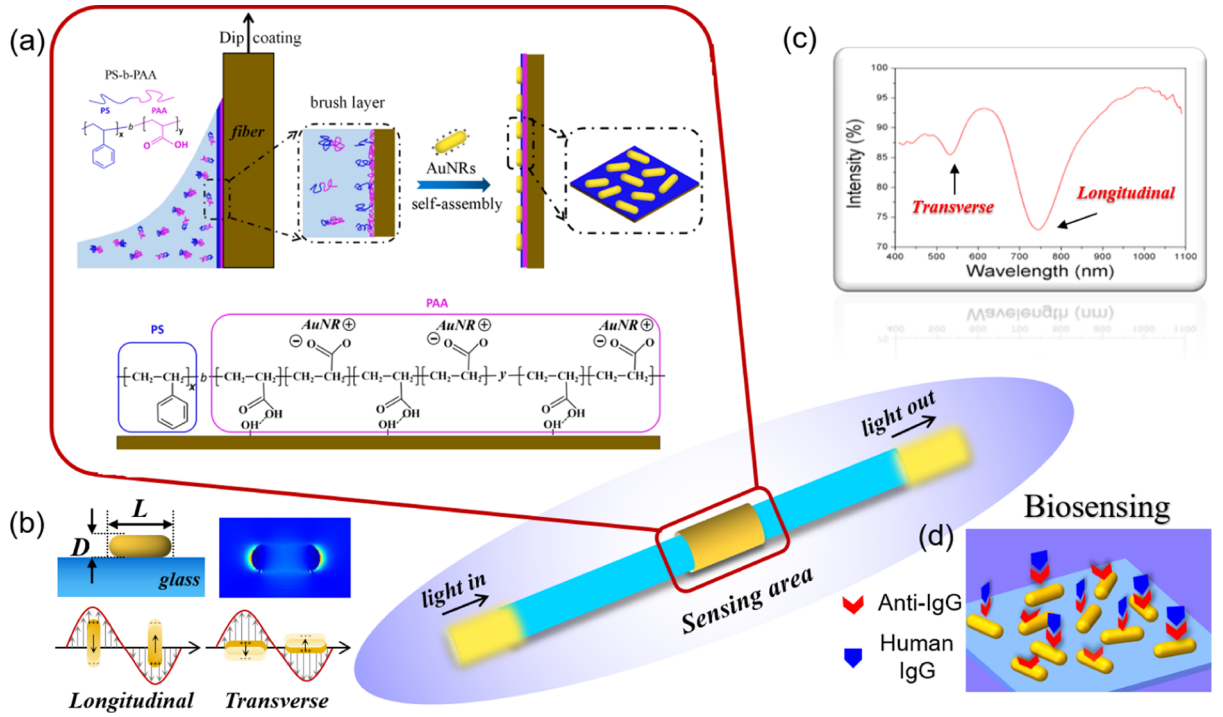

Figure 1. Schematic diagram of the optical fiber-based LSPR sensor. (a) Fabrication process of the LSPR sensors relies on the interaction of the glass-PAA-AuNRs. (b) FDTD simulation and the schematic illustration of LSPR excitation for AuNRs. (c) LSPR transmission bands of AuNRs: LPBs and TPBs corresponding to electron oscillations along the long axis and the short axis of AuNRs, respectively. (d) Biosensing process of human IgG and its antibody.

dipped into the solution at an immersion rate of 20 mm/min, which was followed by a pause of 10 min, and then withdrawn at a controlled rate of 20 mm/min. The dip-coated film was left to dry in a covered container under ambient conditions. The pH and optical density of the AuNR solutions were adjusted to approximately 6 and 3 O.D. (optical density), respectively. The BCP-coated fibers were then incubated in the as-prepared AuNR solutions for 30 min, unless we studied the effect of deposition time. Finally, a 1 min oxygen plasma (plasma cleaner, Hongmin Inc.) treatment was performed at a medium power of 9 W to remove the excess BCP film on the AuNR-assembled fiber.

As the surface of the AuNRs is covered with CTAB molecules that are positively charged, an MPTMS and/or a polyelectrolyte method could also be employed to create the AuNR films for comparison. For the MPTMS method, the hydroxylated fibers were immersed in a 10% (v/v) MPTMS ethanol solution for 12 h and then washed thoroughly with ethanol and ultrapure water. The silanized fiber surface was incubated in the as-prepared AuNR solutions for 2 h to immobilize the particles on the fiber surface *via* S−Au covalent bonds. For the polyelectrolyte method (PDDA/PSS/PAH/PSS multilayer), we followed a process similar to the one we mentioned previously[17] (details in the Supporting Information). All these deposited fibers were stored in a vacuum oven for further use.

Scanning electron microscopy (SEM) (Nova Nano 450, Thermo Scientific Inc.) performed at 5 kV was employed to image the distribution of AuNRs on the fiber surface, while a thin gold film was deposited on the fiber surface to help conduction and electrofocusing.

Experimental Setup. An Ocean Optics HL-2000 light source with a wide wavelength range from 300 to 2000 nm was employed as the illumination light source. The two sides of the sensing region were connected to the source and spectrometer by the fiber couplers. The LSPR transmission spectra were obtained by a fiber spectrometer (HR4000, Ocean Optics Inc.) *via* the real-time data acquisition mode and processed with LabVIEW software. RI sensitivity detection was performed in a flow cell, and the known RI solutions were diluted from a saturated aqueous sucrose solution and measured by an Abbe refractometer.

Finite-Difference Time-Domain Simulation. Commercial finite-difference time-domain (FDTD) software (Lumerical Solutions) was employed to simulate the extinction spectra of the AuNR layers. To perform the calculations, the simulation region was set into a 2 μm cube with the boundary condition of a perfectly matched layer. The AuNRs were represented by hemisphere-capped cylinders with a geometry that matched the SEM image and placed in the center region. The model consisted of AuNRs on silica glass (RI = 1.46), the solution's RI was 1.33, and the size of the particles and their interparticle gaps were varied with experimental requirements. The dielectric constant of gold was obtained from Johnson and Christy's[56] measurements with polynomial fitting, and the light source was set as the total-field scattered-field with an incident angle of 82°.

Antigen−Antibody Interactions of LSPR Biosensors. The AuNR-deposited fiber optic LSPR sensor was further functionalized by covalently immobilizing antihuman IgG on the AuNR surface to create biosensors for human IgG detection. The fabricated process and the details are shown in the Supporting Information. Binding between human IgG and its antibody on the fiber surface thus induces a RI change, further resulting in the resonance wavelength shift necessary for quantitative detection.

Gold Nanoparticle (AuNP)-Enhanced Plasmonic Biosensing of Free *rop* B DNA. Rifampicin-resistant tuberculosis is associated with mutations in the *rop* B gene. The biosensing process of *rop* B DNA consists of a sandwich amplification strategy, and the sequences of the ssDNA are shown in Table S2. First, 3 μM amine-labeled capture ssDNA was fabricated on the AuNR surface through the 11-MUA linker by EDC/NHS activation (as described in the previous section). Free target ssDNA was hybridized with capture ssDNA for 30 min, and the AuNP-probe ssDNA conjugate was then hybridized with target ssDNA for 30 min to enhance the signal. The details of AuNP (12 nm) synthesis and probe ssDNA/AuNP solution preparation are described in the Supporting Information.

Surface-Enhanced Raman Scattering. 4-MBA, a Raman probe, in ethanol was prepared at a concentration of 100 μM. The silicon substrate was treated, cleaned, and hydrolyzed with Piranha solution (H_2SO_4/H_2O_2; 70/30%, beware of strong corrosion!) for 1 h to clean

https://dx.doi.org/10.1021/acsami.0c09711
ACS Appl. Mater. Interfaces XXXX, XXX, XXX−XXX

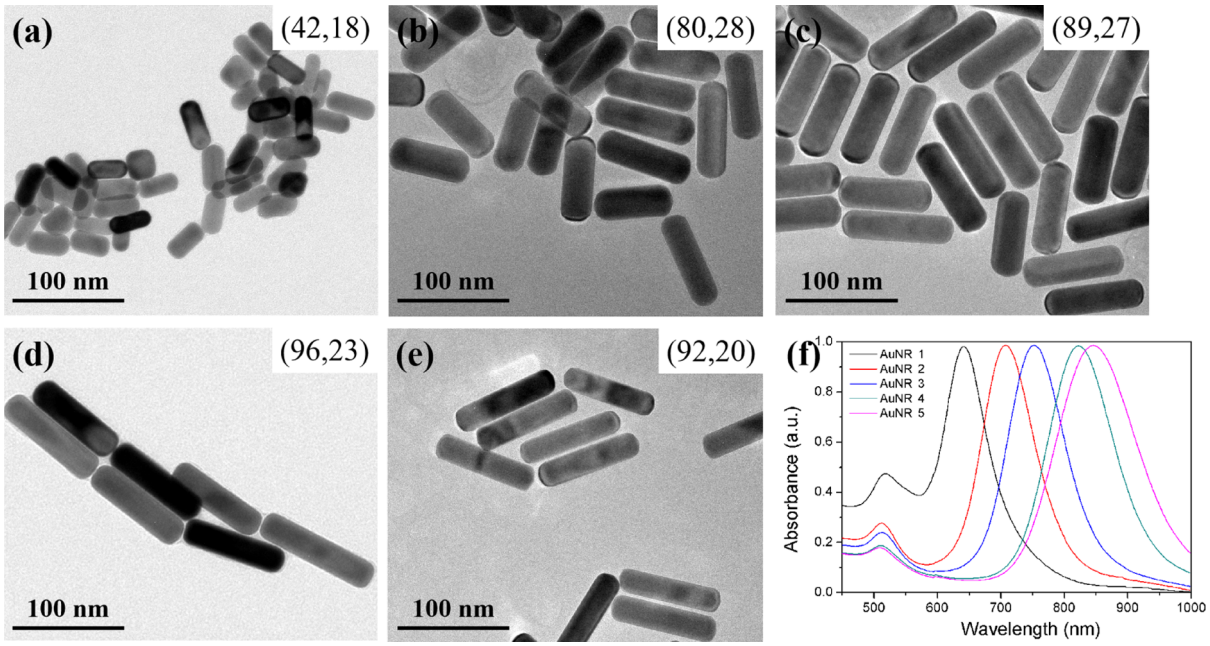

Figure 2. TEM images of AuNR 1 to AuNR 5 with various aspect ratios of (a) 2.33; (b) 2.86; (c) 3.30; (d) 4.17; and (e) 4.60. (f) UV−vis spectra of different sized AuNRs. The length and diameter of AuNRs are shown in the top right corner, and the dimension values were measured in nanometers.

and hydroxylate the surface. After a thorough rinse with water, the substrate was dried in a vacuum oven (100 °C) for 15 min. The BCP templating and AuNR deposition process was same as the process used to prepare the optical fiber LSPR sensor, while the AuNR deposition time was 6 h. The 4-MBA molecules were self-assembled on the AuNR-deposited silicon substrate by immersing the substrate (which was cleaned by oxygen plasma operated at 9 W for 6 min) in the 4-MBA solution overnight. The substrate was then rinsed with ethanol and air-dried for use. All measurements were acquired with an excitation power of 0.75 mW and a 50X microscope objective on a Raman microscope (Renishaw inVia, diode laser-based) operated at 532 nm, and the acquisition time was set to 10 s. All spectra were reported after background subtraction.

RESULTS AND DISCUSSION

Preparation of the AuNR-Based LSPR Sensors. Figure 1 illustrates the configuration of the AuNR-based LSPR sensor. A halogen lamp was employed as the illumination light source, and the AuNRs were excited with an evanescent field, which led to the plasmon resonance bands in the spectrum. The fabrication process of the LSPR sensors relied on the glass-PS-*b*-PAA-AuNR structure, and the dip-coating method of the BCP monolayer and the deposition process of the AuNRs are detailed in the Experimental Section.

The AuNRs we used were synthesized by seed-mediated and surfactant (CTAB)-directed methods, and the homogeneous and adjustable aspect ratio led to a wide LSPR resonance region from the visible region to near-infrared region. In this surfactant-directed synthesis, CTAB acts as both the source of anisotropic growth and the stabilizer. Normally, CTAB molecules could form a cationic bilayer around AuNRs when the concentration was higher than 100 mM, yet they were clearly bound in a weak manner when the concentration of CTAB decreased and then aggregates (below 1 mM). In this case, monodisperse AuNRs with homogeneous shapes (less than 1% shape impurities) could be generated with much lower concentrations of CTAB (lower than 47 mM) and still remained stable after removing the excess CTAB (over 1 mM). The excess CTAB in the solution would disfavor the interaction between AuNRs and PAA chains; however, a lower CTAB concentration also caused aggregation of particles.

Thereby, moderate solution centrifugation and CTAB reduction benefited both the colloidal stability and the deposition process of particles. Figure 2 shows the TEM images of a collection of monodisperse AuNRs synthesized by CTAB and an additive (NaOL or sodium salicylate) in the growth solution. The aspect ratio of nanoparticles was adjusted from 2.33 to 4.60 by varying the amounts of seed solutions, additive, and $AgNO_3$ as well as the pH of growth solutions, and the detailed amounts are listed in Table S1. The average dimensions of two sets of AuNRs, AuNR 1 to AuNR 5, are marked in the top right corners of Figure 2a−e. Figure 2f shows the UV−vis spectra of the AuNR solutions in Figure 2a−e. The corresponding resonance wavelength expectedly red-shifted from 640 to 845 nm as the aspect ratio of the AuNRs increased. In addition, the transverse plasmon bands mainly depended on the diameter of the short axis of AuNRs, which had a small absorption peak at approximately 510 nm in the UV−vis spectra. Both the TEM images and the extinction spectra confirmed the narrow size distribution and high uniformity of the AuNRs, with negligible amount of shape impurities (*e.g.*, spheres).

Herein, we report that the nanothin PS-*b*-PAA films in the form of a brush-like-templated monolayer were suitable for producing dense two-dimensional non-close-packed arrays of AuNRs with little aggregation. The LSPR sensing films were obtained in two simple steps, namely, dipping the noncladded fiber successively in a THF solution of PS-*b*-PAA and, after drying, in an aqueous suspension of CTAB-stabilized AuNRs. The brush-like PS-*b*-PAA monolayer was absorbed to the fiber through multiple noncovalent bonds between Si−OH and the PAA block, which formed the wetting underlayer, whereas the PS block formed a brush-like overlayer. While the deposition

https://dx.doi.org/10.1021/acsami.0c09711
ACS Appl. Mater. Interfaces XXXX, XXX, XXX−XXX

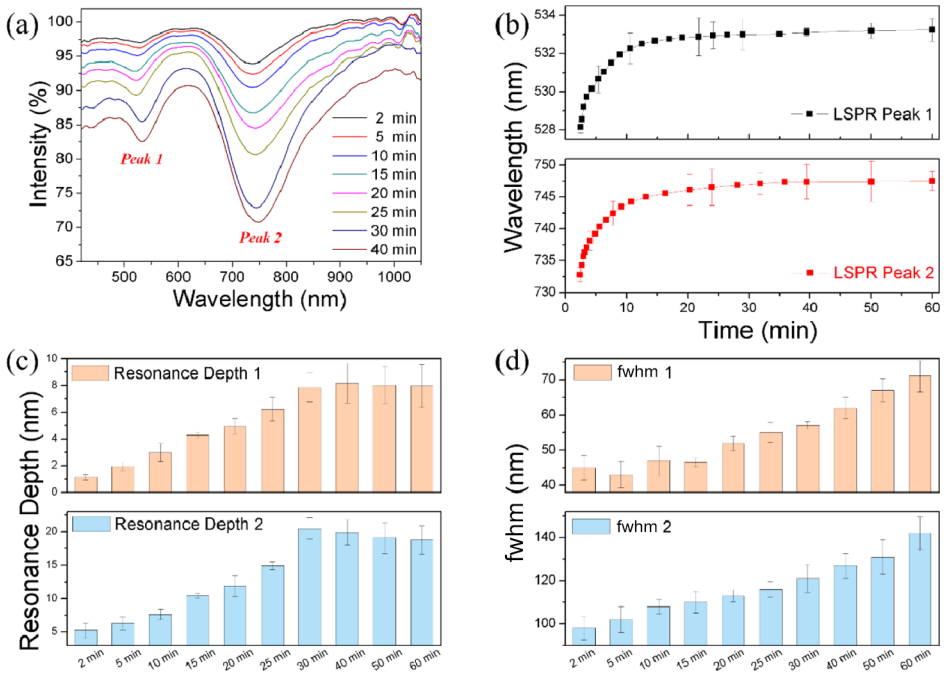

Figure 3. Deposition process of AuNR 2. (a) Real-time normalized LSPR spectra of the AuNR deposition process. The deposition time varied from 2 to 40 min. Peak 1 and peak 2 represent the TPBs and LPBs corresponding to electron oscillations along the long and short axes of AuNRs, respectively. The relationship between (b) peak wavelengths; (c) resonance depths; (d) peak width at half maximums, and the time of AuNR self-assembly.

of AuNRs was directed by electrostatic interactions between AuNRs and deprotonated ionized PAA blocks, the free hydrophobic PS blocks were employed to prevent the aggregation of AuNRs. The pH value of the AuNR solution was adjusted to 6 to favor binding between the PAA block and AuNRs. Most of the hydrophilic carboxylate anions of PAA were ionized in this slightly acidic solution, presenting a negative surface charge opposite of the positive charge of the CTAB-stabilized AuNRs. Hence, the AuNR layers appeared unaffected by AuNR size and led to a well-dispersed and dense AuNR monolayer on the fiber optics.

Refractive Index Sensitivity and Stability of the Fiber Optic LSPR Sensor. To quantify the sensitivity of the AuNR-based LSPR fiber sensors to bulk RI variations, solutions with increasing sucrose concentrations and known RIs (from 1.32 to 1.37) were successively injected into the flow cell, while the transmitted optical signal was synchronously recorded. Two plasmon bands were evident in the transmission spectrum of the AuNRs and associated with the longitudinal plasmon band (LPB) and the transverse plasmon band (TPB), corresponding as they did to electron oscillation along the long and short axes of the AuNR, respectively. Taking the LSPR sensor functionalized with AuNR 2 as an example, Figure 3 shows the LSPR spectrum characteristics during the deposition process. According to the real-time normalized transmission spectra in Figure 3a, we recorded both the TPBs (peak 1) and the LPBs (peak 2) in the AuNR 2 aqueous solution at different deposition times. The wavelength of peak 1 had a series of slight red shifts when the deposition time increased from 0 to 20 min and then reached a plateau (Figure 3b). A similar trend was observed for peak 2, where the wavelength exhibited a large red shift from 732 to 747 nm in the first 30 min and then once again reached a plateau. This red shift is an indication that the dielectric environment changed in the deposition process and putatively assigned to adsorption to the polymer and the increasing density of AuNRs on the surface. Meanwhile, the resonance depths of the two peaks, which are correlated to the density of AuNRs, were also studied. As shown in Figure 3c, the depths of the plasmon resonances also increased rapidly until the deposition time increased to 30 min and then appeared to slightly decrease for longer times. The full width at half-maximum (fwhm) of the two peaks increased steadily with increasing deposition time (Figure 3d), which leads to higher signal noise and lower RI resolution. Hence, the AuNR 2 deposition time of 30 min offered fibers with the best optical properties (high sensitivity, low signal noise, narrow fwhm, and deep peak depth).

To verify whether the AuNR aspect ratio influenced the deposition of AuNRs on the PS-*b*-PAA brush-like monolayer, the other four sizes of particles were tested (Figures S2−S5). Different aspect ratios of AuNRs had similar LSPR spectrum characteristics during the deposition process. Generally, a deposition time of 30 min led to fibers with the best optical properties although the resonance red-shifted at longer deposition times for larger aspect ratio AuNRs. Here, to further compare the properties of the AuNR-based LSPR sensors with different aspect ratios, a uniform deposition time of 30 min was set for the remaining experiments.

Next, their RI sensitivities were evaluated. For the spectra of the AuNR-based LSPR sensor, the spectral resonance depth decreased with increasing RI. The TPB of AuNRs was nearly insensitive to the changes in the size of the AuNRs and the surrounding RIs (Figure 4), whereas the LPB showed a red shift with the increase in the aspect ratio of AuNRs and a concurrent increase in RI sensitivity. Therefore, a peak wavelength 1 (LPB) was chosen to evaluate and compare the RI sensitivities of the LSPR sensors functionalized with AuNRs having different aspect ratios. The LSPR sensor based on the AuNRs with the largest aspect ratio of 4.60 led to the highest sensitivity of 753 nm/RIU, which decreased to 195

https://dx.doi.org/10.1021/acsami.0c09711
ACS Appl. Mater. Interfaces XXXX, XXX, XXX−XXX

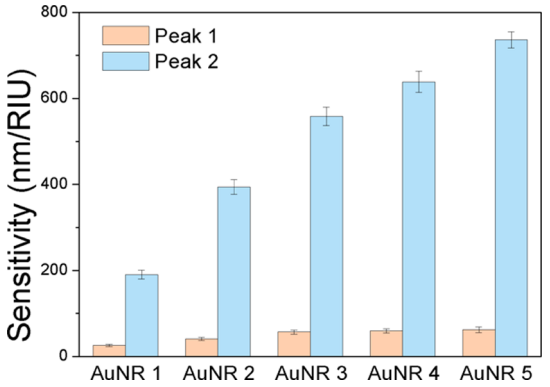

Figure 4. Refractive index sensitivity of the LSPR peak wavelength shifts for different sizes of particles at a deposition time of 30 min.

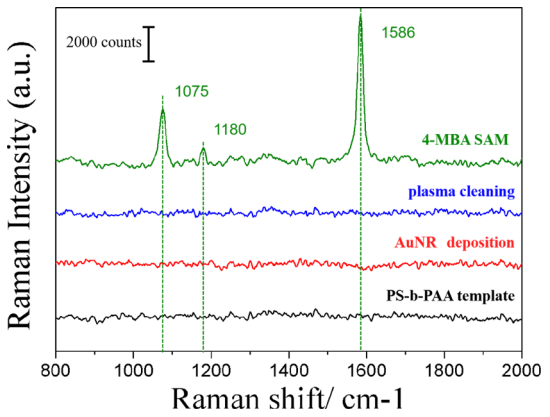

Figure 5. SERS spectra of 100 μM 4-MBA on various substrates. The major SERS bands are marked by dashed lines, and the substrates are shown in different colors on the right.

nm/RIU for the sensor functionalized by AuNRs with an aspect ratio of 2.33. Furthermore, the stability of the PS-*b*-PAA brush-like monolayer-based AuNR LSPR sensor was studied under different conditions (Figure S6). The peak wavelength of the sensor shown in Figure S6a was measured in a series of saline solutions for 10 min each, and the concentration of saline solution was increased from 0 to 26 wt % (saturated solution) and then decreased back to 0. The response remained stable, even in the saturated saline solution, and was found to be consistent under the same conditions. The peak wavelength response to PBS solutions with different pHs was also measured and is shown in Figure S6b. The response remained stable at different pHs (varied from 4.0 to 10.0), and the peak wavelength slightly blue-shifted with the increasing pH value. The long-term stability of the PS-*b*-PAA brush-like monolayer-based AuNR LSPR sensor was followed by measuring the peak wavelength response to PBS solution (pH = 7.4). The response was found to remain the same for 10 days (Figure S7) even after prolonged storage for a month, indicating the good long-term stability of the fabricated LSPR sensor. Excellent stability under both long-term and different conditions indicated that the PS-*b*-PAA brush-like monolayer-based AuNR surface was structurally stable and free of morphological changes.

Surface-Enhanced Raman Scattering Performance of PS-B-PAA-Templated AuNR Nanostructures. Next, the optical properties of the PS-*b*-PAA-templated AuNR nanostructure were characterized by determining the surface-enhanced Raman scattering (SERS) performance on a silicon substrate that was oxidized to silicon dioxide. In Figure 5, there is no clear Raman band observed from the PS-*b*-PAA template, probably because of the lack of SERS enhancement obtained for the nano-thin-film template left underneath the nanoparticles. No extra peaks appeared after CTAB-stabilized AuNR deposition in this SERS detection range. Then, the exposed CTAB and PS-*b*-PAA on the surface were completely removed by the plasma treatment, but the polymer that connected with the AuNRs mostly survived the plasma process as the particles were still stable on the substrate thereafter. Finally, the 4-MBA-modified PS-*b*-PAA-templated AuNR nanostructures exhibited high-intensity 4-MBA characteristic peaks at 1586 and 1075 cm^{-1} and a relatively weak mode at 1180 cm^{-1}. In addition, no characteristic peak of 4-MBA was obtained when the 4-MBA solution was dried on the substrate. This enhanced response on the PS-*b*-PAA-templated AuNR nanostructure demonstrated that our polymer-templated particle monolayers also have excellent potential for SERS enhancement applications.

Biosensing Applications of the Fiber Optic LSPR Sensor. To investigate the performance of the AuNR-based LSPR biosensors, both IgG detection by antigen−antibody interactions and free ssDNA hybridization detection were used here. For the antigen−antibody interaction, the AuNRs immobilized on the fiber surface were further functionalized with antihuman IgG *via* the 11-MUA linker. Afterward, the biomolecular binding process and the corresponding spectrum changes were monitored and recorded. As expected, higher concentrations of human IgG yielded greater shifts in peak wavelength, with the observation of a Langmuir isotherm with a plateau (Figure 6). This occurred because the antigen−

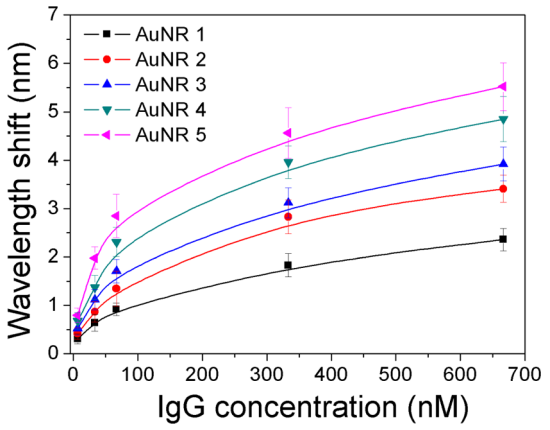

Figure 6. Calibration curve of the LSPR peak wavelength with the different concentrations of human IgG for different sizes of particles.

antibody binding taking place at a higher concentration of human IgG resulted in a greater change in the RI at the AuNR-based fiber surface. For all concentrations, the LSPR sensor based on AuNRs with an aspect ratio of 4.60 (AuNRs 5) had the largest response, which indicated that the LSPR sensor functionalized with the larger aspect ratio AuNRs had a higher sensitivity. This performance was also consistent with the results previously obtained in RI sensitivity detection. In addition, the limit of detection (LOD) calculated for the LSPR biosensors functionalized with AuNRs 1, 2, 3, 4, and 5 was 2.6, 2.0, 1.7, 1.1, and 0.8 nM, respectively. Reproducibility is a

https://dx.doi.org/10.1021/acsami.0c09711
ACS Appl. Mater. Interfaces XXXX, XXX, XXX−XXX

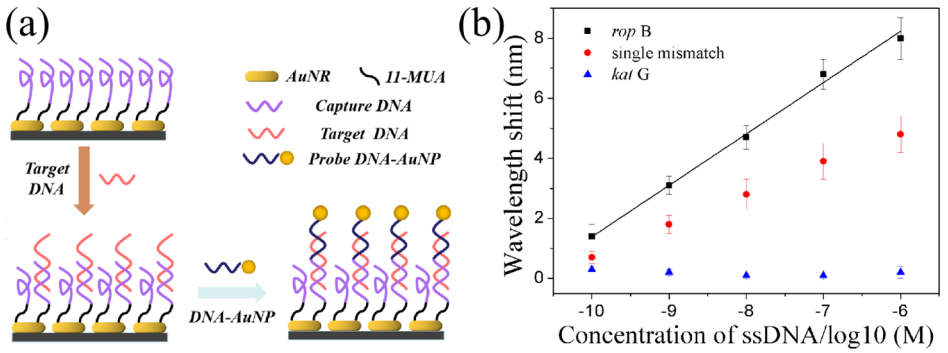

Figure 7. DNA hybridization analyses by AuNP amplification. (a) Schematic diagram of AuNP-enhanced plasmonic biosensing of sandwich DNA hybridization. (b) Peak wavelength shift after AuNP-DNA hybridization with various concentrations of *rop* B, single mismatch *rop* B, and *kat* G.

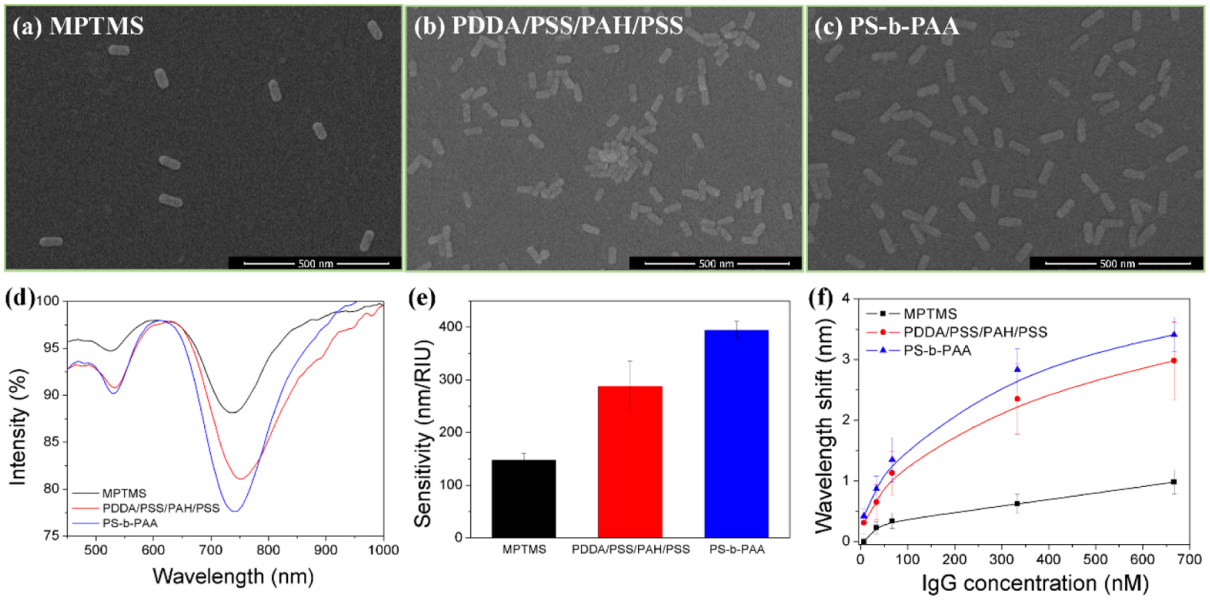

Figure 8. SEM images of AuNRs immobilized on the optical fiber through (a) MPTMS; (b) PDDA/PSS/PAH/PSS; and (c) PS-*b*-PAA monolayer methods. (d) Comparison of the absorption spectra of the AuNR-assembled films prepared by different deposition methods. (e) Refractive index sensitivity of the LSPR peak wavelength. (f) Calibration curves obtained for IgG using three different deposition methods under otherwise identical conditions.

major requirement of a reusable biosensor. The same immobilized surface could be used for a series of measurements *via* regeneration with glycine-HCl buffer (pH = 2) for 1 min. Under these conditions, the surface could be regenerated while maintaining the activity of the antibodies for the next rounds of antigen−antibody interaction measurements. Figure S8 shows the 10 replicates of IgG detection performed at 333.4 nM, and the results revealed that the biosensor has satisfactory repeatability with a relative standard deviation of 3.9%. Note that the signal gradually and slightly decreased (less than 10%) as the number of regeneration cycles increased because of the incomplete elution of a small amount of IgG.

Moreover, a sandwich hybridization strategy was established for analyzing free *rop* B ssDNA. The capture strand consisting of half the sequence complementary to *rop* B DNA was immobilized on the LSPR biosensor (AuNR 2-based sensor), and the other half of the complementary sequence was immobilized on the AuNPs to enhance the sensing signal (Figure 7a). Figure 7b shows a good linearity (R^2 = 0.995) between peak wavelength shift and *rop* B concentration in the range of 10^{-10} to 10^{-6} M. The LOD of rop B was estimated to be approximately 29 pM. As a negative control, single mismatch ssDNA of *rop* B and noncomplementary ssDNA (*kat* G) were analyzed under the same conditions. The peak wavelength shift of single mismatch ssDNA was lower than that of the complementary *rop* B ssDNA because of the weaker specific binding, while very little nonspecific adsorption occurred from the noncomplementary ssDNA (*kat* G). In addition, the AuNPs used for surface enhancement did not alter the LSPR sensing spectral waveform but only caused peak wavelength shift (Figure S9). Hence, these examples show that the AuNR-based LSPR fiber sensors prepared by the PS-*b*-PAA brush-like monolayer are excellent platforms for the sensitive and label-free biosensing of biomolecules.

Comparison with Other AuNR Deposition Methods. The BCP dip-coating method (PS-*b*-PAA monolayer) we used in this study was distinct from the traditional methods of silane coupling (MPTMS) and layer-by-layer polyelectrolyte (PDDA/PSS/PAH/PSS)-induced assembly of AuNRs. To compare these methods, the surface morphology of the assembled AuNRs, LSPR spectrum, RI sensitivity, and the biosensing application were monitored (Figure 8). Here, we used AuNR 2 as the comparative nanostructure. SEM images of the three deposition methods indicated that the geometric

https://dx.doi.org/10.1021/acsami.0c09711
ACS Appl. Mater. Interfaces XXXX, XXX, XXX−XXX

distribution of particles on the PS-*b*-PAA brush-like monolayer was well dispersed with high coverage; however, the layer-by-layer polyelectrolytes led to highly localized particle aggregates, and the MPTMS monolayer caused a large reduction in the AuNR density (Figure 8a–c). The absorption spectra of the AuNRs in water showed the best optical properties (the peak depth was 21%, and the fwhm was 115 nm) with the PS-*b*-PAA template (Figure 8d). The peak depth was 10 and 17% for the MPTMS and polyelectrolytes methods, respectively. Comparatively, the fwhm was 107 and 126 nm for the MPTMS and polyelectrolytes methods, respectively. The RI sensitivity of the AuNRs on the PS-*b*-PAA brush-like monolayer-based fiber sensor was approximately 2.7 times higher than that of the AuNRs on MPTMS and 1.4 times higher than that of the AuNRs on polyelectrolytes (Figure 8e). The human IgG biosensing test was also performed for comparison (Figure 8f). The LOD of the PS-*b*-PAA-based sensors functionalized by AuNR 2 was calculated to be 2.0 nM. Comparatively, the LOD of MPTMS and polyelectrolytes was 9.3 and 2.5 nM, respectively, indicating a poorer performance than that of the PS-*b*-PAA-based sensors.

The developed LSPR biosensor was used for the determination of human IgG in human serum. As the high concentration of IgG in the stock serum (76 μM) could saturate the signal, the serum was diluted in PBS to obtain an IgG concentration of 333.4 nM. The peak wavelength responses of the AuNR-based LSPR biosensors, which were fabricated by three deposition methods, are shown in Table 1.

Table 1. LSPR Biosensor Response of Human IgG (333.4 nM) in Both PBS Solution and Human Serum

	PS-*b*-PAA (nm)	MPTMS (nm)	PDDA/PSS/PAH/PSS (nm)
IgG in PBS	2.83 ± 0.35	0.62 ± 0.16	2.35 ± 0.48
IgG in human serum	3.11 ± 0.38	0.91 ± 0.28	3.58 ± 0.31

The response in serum was higher than that in PBS because of nonspecific adsorption in serum. The PS-*b*-PAA method (9%) resulted in much less nonspecific adsorption than the MPTMS method (47%) and PDDA/PSS/PAH/PSS method (52%). According to the calibration curves in Figure 8f (obtained in PBS solution), the corresponding IgG concentrations in serum were estimated to be 505, 602, and >667 nM (exceeds the calibration range) for the PS-*b*-PAA-, MPTMS-, and PDDA/PSS/PAH/PSS-based biosensors, respectively. Thereby, compared with biosensors prepared by other methods, the PS-*b*-PAA monolayer-based LSPR biosensor has a more accurate response and a lower nonspecific adsorption in real serum sample detection.

To demonstrate the specific antibody–antigen recognition ability of the PS-*b*-PAA-templated AuNR LSPR biosensor proposed in this work, a comparison of the detection limit shows that the current biosensor exhibits a better performance than sensors prepared by other plasmonic methods for IgG immunosensing (Table 2). In addition, this PS-*b*-PAA-templated deposition method is much simpler and more effective than other methods. Compared to the AuNP-based LSPR biosensor we previously reported,[17] both the AuNP- and AuNR-deposited LSPR biosensors were based on wavelength interrogation. Specifically, by manipulating the aspect ratio of AuNRs, the LPB wavelength of the AuNR-based LSPR sensor can be conveniently regulated throughout the visible and near-infrared regions and into the infrared region, allowing the LSPR sensor to be applied to particular applications where a specific wavelength and high RI sensitivity are desired. For example, the working wavelength of the tilted fiber Bragg grating (TFBG) is in the infrared region, but the spherical gold particles cannot excite LSPR in this wavelength region. However, the LSPR excitation wavelength of gold nanorods could be adjusted to the infrared region for TFBG LSPR sensor applications. As such, AuNRs offer much more flexibility than spherical Au nanoparticles. A similar situation also occurs in phase-interrogated LSPR sensors. Thereby, gold nanorods have a higher sensitivity and wider applications than gold particles because of their adjustable interrogation wavelength.

Table 2. Comparison of the LODs of Optical Fiber Biosensors Prepared by Different Methods

method	analyte	LOD (nM)	refs
TFBG SPR	human IgG	3.3	57
PC SPR	antibovine IgG	1.8	58
LMR	antigoat IgG	9.9	59
AuNP LSPR	antihuman IgG	1.6	21
U-bent AuNP LSPR	antihuman IgG	0.8	16
AuNR LSPR	antihuman IgG	3	60
AuNR LSPR	human IgG	0.8	this work

The results presented above demonstrate that the use of the PS-*b*-PAA brush-like monolayer to deposit AuNRs on optical fibers improves surface coverage, reduces particle aggregation, and further enhances RI sensitivity and biosensing capability. In addition, the sensing performance could also be further improved by optimizing the key parameters of the fiber sensor, such as the aspect ratio or deposition time of the AuNRs. Thereby, in this case, the factors that affected the sensitivity of the sensors were analyzed by both experiments and simulations in the next section.

Effect of the Deposition Time and Aspect Ratio of AuNRs. The deposition process of AuNRs on the PS-*b*-PAA brush-like monolayer was further investigated with a series of SEM images obtained with various deposition times and different aspect ratios of AuNRs. We first varied the deposition time of fibers in the AuNR 2 solution and observed a series of AuNR coverage, as shown in the SEM images (Figure 9). With longer deposition times, the coverage of AuNRs increased significantly to 12.7% (Figure S10). The greater AuNR coverage achieved with longer deposition times resulted in a stronger plasmon band and then caused the peaks to red shift and RI sensitivity to increase. The SEM images were in agreement with the LSPR spectrum characteristics shown in Figure 4. The aggregation of AuNRs augmented with the deposition time after 30 min, which caused an increase in the fwhm and slight decrease in resonance depth.

To further investigate the self-assembly of AuNRs on the PS-*b*-PAA brush-like monolayer (Figure S11), whether the size of AuNRs influenced their deposition on the surface was determined. Note that the deposition time was held constant at 30 min for all the sizes for comparison. The AuNR density decreased, as expected, with an increase in the aspect ratio of AuNRs (from close to 100 to approximately 60 AuNR/μm^2, which was calculated from Figure S10).

To better understand the plasmon resonance response of the AuNRs on the optical fibers, the influence of factors, such as the shape, size, and distance of nanoparticles, was simulated.

https://dx.doi.org/10.1021/acsami.0c09711
ACS Appl. Mater. Interfaces XXXX, XXX, XXX–XXX

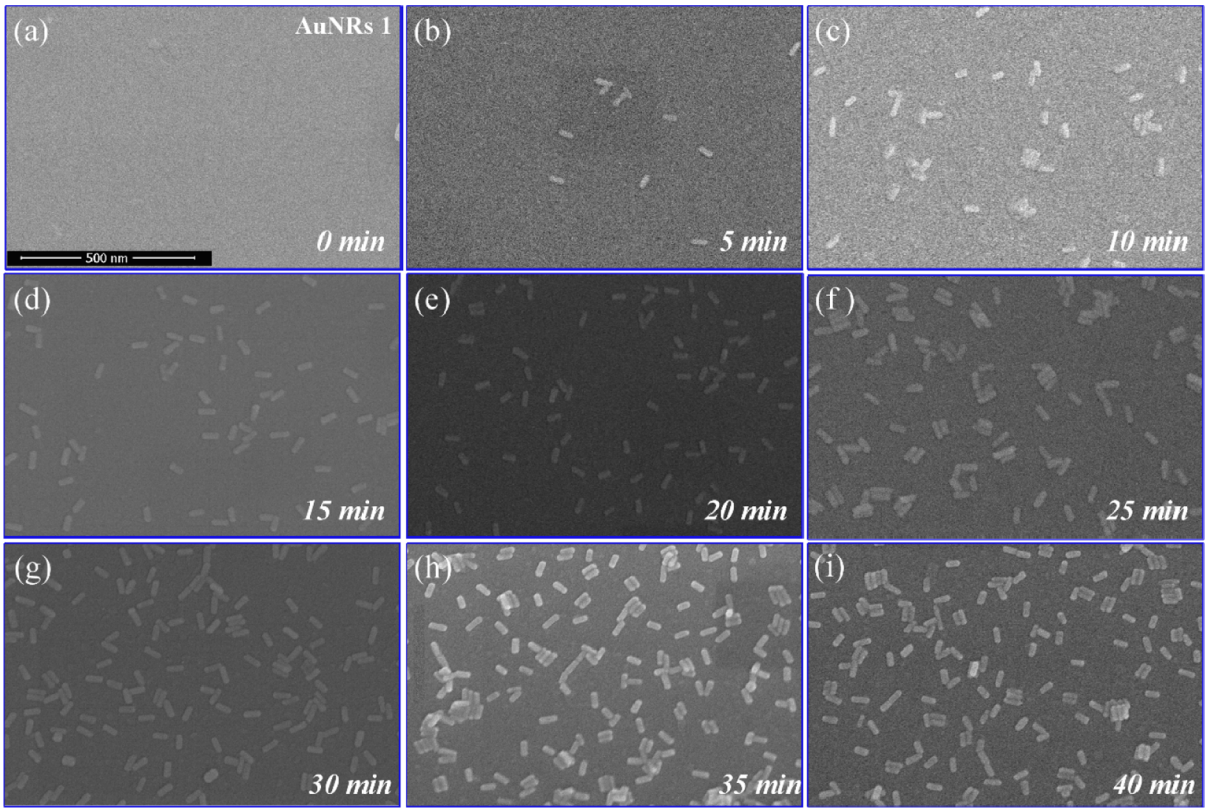

Figure 9. SEM images of the AuNR 2 distribution with different deposition times on the PS-*b*-PAA surface. The deposition time varied from 0 to 40; (a) 0; (b) 5; (c) 10; (d) 15; (e) 20; (f) 25; (g) 30; (h) 35; and (i) 40 min. The scale bar (500 nm) provided in (a) applies uniformly.

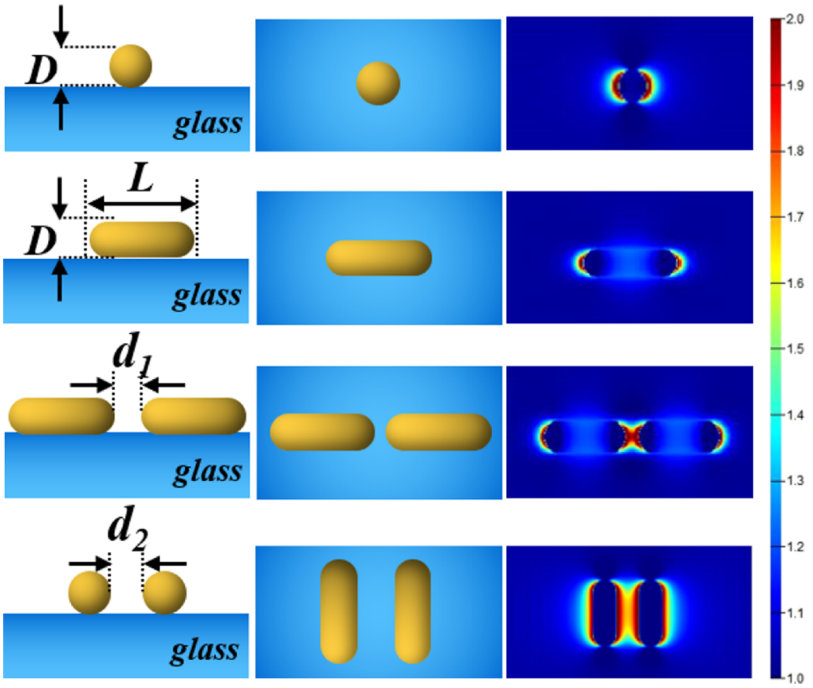

Figure 10. Single and coupled AuNPs and AuNRs modeled with FDTD simulations and the corresponding electric field distributions.

We employed the FDTD algorithm to properly model the interaction of AuNRs with EM radiation and calculate the electric field variation and absorption spectrum of immobilized AuNRs surrounded by different RI dielectrics. The geometry and orientation (the first column shows the *XZ* plane, and the second column shows the *XY* plane) of FDTD modeling and the resultant EM field distribution at the equatorial *XY* plane of AuNPs and AuNRs (the third column) are shown in Figure 10. We also examined the response of different types of coupled AuNRs, namely, T-type (transverse to transverse in the third row, d_1 = 5 nm) and L-type (longitudinal to longitudinal in the fourth row, d_2 = 5 nm). Compared with that of a single AuNP,

https://dx.doi.org/10.1021/acsami.0c09711
ACS Appl. Mater. Interfaces XXXX, XXX, XXX−XXX

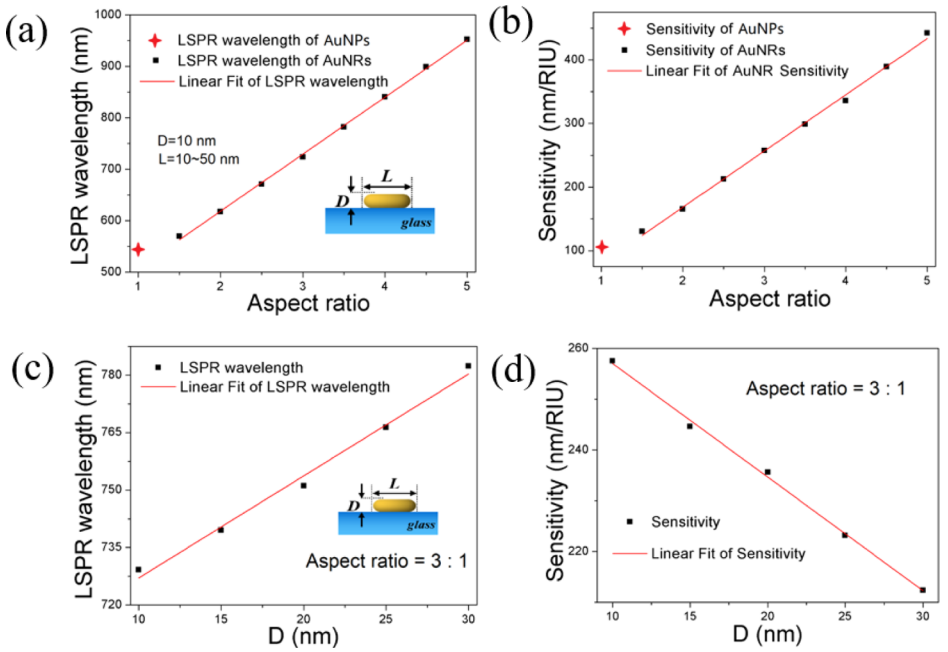

Figure 11. Results obtained from the FDTD simulations of a single AuNR on SiO_2 glass in aqueous solutions (n = 1.33−1.43). (a) Linear relationship between the aspect ratio of an AuNR (D = 10 nm) and the longitudinal peak wavelength. (b) RI sensitivity of the longitudinal peak wavelength with different aspect ratios. The red star shows the AuNP with a diameter of 10 nm. Calibration curve of (c) longitudinal peak wavelengths and (d) their sensitivities with varied lengths of D for an AuNR aspect ratio of 3:1.

the strong EM fields of a single AuNR were mainly distributed on the ends of the nanorods. If two AuNRs were close enough to interact electromagnetically with each other, their LSPR peaks shift from the single-NR peak position because of surface plasmon coupling. Note that T-type coupled AuNRs caused a red shift of the plasmon band, whereas L-type coupled AuNRs led to a blue shift. The closer the neighboring AuNRs were, the stronger the surface plasmon coupling that would be obtained, which caused a larger LSPR peak shift and an increase in the fwhm. Hence, through the effective control of the nanoparticle spacing, the LSPR spectra and peak positions could be optimized to enhance sensitivity and resolution. This standpoint was further supported by the experimental results obtained with different AuNR immobilization methods, as presented in the next section.

In addition to varying the shape and spacing of the nanoparticles, we also simulated a single AuNR on SiO_2 glass with varied diameters (D) and aspect ratios (L/D), as shown in Figure 11. As shown in Figure 11a, with D constant at 10 nm, the calculated longitudinal peak wavelengths were plotted as a function of the aspect ratio of the AuNR (10−50 nm). The peak wavelength red-shifted linearly as the aspect ratio of the AuNR increased. The corresponding RI sensitivity simulation is shown in Figure 11b, revealing that the RI sensitivity increased linearly with increasing the aspect ratio of AuNRs. Moreover, the calibrated linear curves of the longitudinal peak wavelengths and their sensitivities with varied lengths of D are shown in Figure 11c,d, respectively. In particular, the aspect ratio was a constant of 3:1. The peak wavelength red-shifted from 729 to 782 nm, while the corresponding RI sensitivity slightly decreased when the width of D increased from 10 to 30 nm. The estimated abovementioned results agreed well with our experimental results and also directed parameter (the diameter and aspect ratio of AuNRs) optimization to enhance the sensitivity and stability of the LSPR sensors.

CONCLUSIONS

In summary, an optical fiber-based LSPR biosensor was fabricated by the self-assembly of CTAB-stabilized AuNRs on a PS-*b*-PAA brush-like template and exhibited increased sensitivity for RI sensing for applications including protein immunoassays, DNA biosensing, and SERS detection. The studies presented here illustrated the feasibility of fabricating our polymer-templated optical fiber sensors with AuNRs having varied aspect ratios and controlling the LSPR peak wavelength for biochemical sensing. Both the experimental and simulation results suggested that the deposition time, particle aspect ratio, coverage, and interparticle gap all affected the optical properties of the proposed optical fiber-based LSPR sensors. In theory, with decreasing the T-type interparticle gap, the LSPR peak wavelength red-shifted, and the correlative RI sensitivity increased, while decreasing the L-type interparticle gap obtained opposite results. The AuNRs with larger aspect ratios needed long deposition times to obtain better optical sensing performances while leading to higher RI sensitivity and a lower LOD for biosensing. The highest sensitivity of the sensor was 753 nm/RIU, and the detection limit of the biosensor for human IgG and the free ssDNA of *rop* B were 0.8 nM and 29 pM, respectively. Furthermore, comparing the optical performances of other self-assembly methods showed that the PS-*b*-PAA brush-like monolayer led to high coverage and well-dispersed AuNR layers for high sensitivity biosensing. Comparing with classical methods of fabricating AuNP-based LSPR sensors showed that the PS-*b*-PAA brush-like monolayer self-assembled AuNR fiber LSPR sensors had a tunable wavelength detection range and great potential for biomolecule monitoring in on-site applications. Thus, this study furthered

https://dx.doi.org/10.1021/acsami.0c09711
ACS Appl. Mater. Interfaces XXXX, XXX, XXX−XXX

the development of a simple, efficient, wavelength-adjustable, and sensitive optical fiber LSPR sensor.

■ ASSOCIATED CONTENT

Supporting Information

The Supporting Information is available free of charge at https://pubs.acs.org/doi/10.1021/acsami.0c09711.

Experimental details of biosensor preparation; synthetic condition of AuNRs; sequences of DNA; UV−vis spectra; deposition process, stability, and repeatability studies; and surface coverage evaluation (PDF)

■ AUTHOR INFORMATION

Corresponding Authors

Jean-Francois Masson − *Département de Chimie, Regroupement Québécois des Matériaux de Pointe, and Centre Québécois sur les Matériaux Fonctionnels (CQMF), Université de Montréal, Montreal H3C 3J7, Quebec, Canada;* orcid.org/0000-0002-0101-0468; Email: jf.masson@umontreal.ca

Wei Peng − *College of Physics, Dalian University of Technology, Dalian 116024, China;* orcid.org/0000-0002-0246-0698; Email: wpeng@dlut.edu.cn

Authors

Mengdi Lu − *College of Physics, Dalian University of Technology, Dalian 116024, China;* orcid.org/0000-0001-6526-1955

Hu Zhu − *Department of Chemistry, University of Toronto, Ontario M5S3H6, Canada*

Long Hong − *School of Life Sciences, Peking University, Beijing 100871, China*

Jijun Zhao − *College of Physics, Dalian University of Technology, Dalian 116024, China;* orcid.org/0000-0002-3263-7159

Complete contact information is available at: https://pubs.acs.org/10.1021/acsami.0c09711

Notes

The authors declare no competing financial interest.

■ ACKNOWLEDGMENTS

We acknowledge funding from the National Natural Science Foundation of China (NSFC) (grant nos. 61727816, 61520106013, and 11474043), the Postdoctoral Science Foundation of China (grant no. 2019M661092), and the Natural Science and Engineering Research Council (NSERC) of Canada (grant no. RGPIN/03864-2016).

■ REFERENCES

(1) Haes, A. J.; Van Duyne, R. P.; Duyne, V. A Unified View of Propagating and Localized Surface Plasmon Resonance Biosensors. *Anal. Bioanal. Chem.* **2004**, *379*, 920−930.

(2) Chung, T.; Lee, S.-Y.; Song, E. Y.; Chun, H.; Lee, B. Plasmonic Nanostructures for Nano-Scale Bio-Sensing. *Sensors* **2011**, *11*, 10907−10929.

(3) Jin, R.; Charles Cao, Y.; Hao, E.; Métraux, G. S.; Schatz, G. C.; Mirkin, C. A. Controlling Anisotropic Nanoparticle Growth through Plasmon Excitation. *Nature* **2003**, *425*, 487−490.

(4) Pattnaik, P. Surface Plasmon Resonance: Applications in Understanding Receptor-ligand Interaction. *Appl. Biochem. Biotechnol.* **2005**, *126*, 79−92.

(5) Masson, J.-F. Surface Plasmon Resonance Clinical Biosensors for Medical Diagnostics. *ACS Sens.* **2017**, *2*, 16−30.

(6) Cao, J.; Sun, T.; Grattan, K. T. V. Gold Nanorod-Based Localized Surface Plasmon Resonance Biosensors: A review. *Sens. Actuators, B* **2014**, *195*, 332−351.

(7) Wang, S.; Li, W.; Chang, K.; Liu, J.; Guo, Q.; Sun, H.; Jiang, M.; Zhang, H.; Chen, J.; Hu, J. Localized Surface Plasmon Resonance-Based Abscisic Acid Biosensor Using Aptamer-Functionalized Gold Nanoparticles. *Plos One* **2017**, *12*, No. e0185530.

(8) Homola, J.; Koudela, I.; Yee, S. S. Surface Plasmon Resonance Sensors Based on Diffraction Gratings and Prism Couplers: Sensitivity Comparison. *Sens. Actuators, B* **1999**, *54*, 16−24.

(9) Karlsson, R. SPR for Molecular Interaction Analysis: A Review of Emerging Application Areas. *J. Mol. Recognit.* **2004**, *17*, 151−161.

(10) Zhao, S. S.; Bukar, N.; Toulouse, J. L.; Pelechacz, D.; Robitaille, R.; Pelletier, J. N.; Masson, J.-F. Miniature Multi-Channel SPR Instrument for Methotrexate Monitoring in Clinical Samples. *Biosens. Bioelectron.* **2015**, *64*, 664−670.

(11) Säfsten, P.; Klakamp, S. L.; Drake, A. W.; Karlsson, R.; Myszka, D. G. Screening antibody-antigen interactions in parallel using Biacore A100. *Anal. Biochem.* **2006**, *353*, 181−190.

(12) Tagit, O.; Hildebrandt, N. Fluorescence Sensing of Circulating Diagnostic Biomarkers Using Molecular Probes and Nanoparticles. *ACS Sens.* **2017**, *2*, 31−45.

(13) Caucheteur, C.; Guo, T.; Albert, J. Review of Plasmonic Fiber Optic Biochemical Sensors: Improving the Limit of Detection. *Anal. Bioanal. Chem.* **2015**, *407*, 3883−3897.

(14) Masson, J.; Obando, L.; Beaudoin, S.; Booksh, K. Sensitive and real-time fiber-optic-based surface plasmon resonance sensors for myoglobin and cardiac troponin I. *Talanta* **2004**, *62*, 865−870.

(15) Pollet, J.; Delport, F.; Janssen, K. P. F.; Jans, K.; Maes, G.; Pfeiffer, H.; Wevers, M.; Lammertyn, J. Fiber Optic SPR Biosensing of DNA Hybridization and DNA-Protein Interactions. *Biosens. Bioelectron.* **2009**, *25*, 864−869.

(16) Sai, V. V. R.; Kundu, T.; Mukherji, S. Novel U-bent Fiber Optic Probe for Localized Surface Plasmon Resonance Based Biosensor. *Biosens. Bioelectron.* **2009**, *24*, 2804−2809.

(17) Lu, M.; Zhu, H.; Bazuin, C. G.; Peng, W.; Masson, J.-F. Polymer-Templated Gold Nanoparticles on Optical Fibers for Enhanced-Sensitivity Localized Surface Plasmon Resonance Biosensors. *ACS Sens.* **2019**, *4*, 613−622.

(18) Haes, A. J.; Duyne, R. P. V. Preliminary Studies and Potential Applications of Localized Surface Plasmon Resonance Spectroscopy in Medical Diagnostics. *Expert Rev. Mol. Diagn.* **2004**, *4*, 527−537.

(19) Lee, S.; Pérez-Luna, V. H. Dextran−Gold Nanoparticle Hybrid Material for Biomolecule Immobilization and Detection. *Anal. Chem.* **2005**, *77*, 7204−7211.

(20) Huang, H.; Tang, C.; Zeng, Y.; Yu, X.; Liao, B.; Xia, X.; Yi, P.; Chu, P. K. Label-free Optical Biosensor Based on Localized Surface Plasmon Resonance of Immobilized Gold Nanorods. *Colloids Surf., B* **2009**, *71*, 96−101.

(21) Cao, J.; Tu, M. H.; Sun, T.; Grattan, K. T. V. Wavelength-based Localized Surface Plasmon Resonance Optical Fiber Biosensor. *Sens. Actuators, B* **2013**, *181*, 611−619.

(22) Kumar, S.; Kaushik, B. K.; Singh, R.; Chen, N.-K.; Yang, Q. S.; Zhang, X.; Wang, W.; Zhang, B. LSPR-Based Cholesterol Biosensor Using A Tapered Optical Fiber Structure. *Biomed. Opt. Express* **2019**, *10*, 2150−2160.

(23) Zhang, Z.; Chen, Z.; Qu, C.; Chen, L. Highly Sensitive Visual Detection of Copper Ions Based on the Shape-Dependent LSPR Spectroscopy of Gold Nanorods. *Langmuir* **2014**, *30*, 3625−3630.

(24) Jia, S.; Bian, C.; Sun, J.; Tong, J.; Xia, S. A Wavelength-Modulated Localized Surface Plasmon Resonance (LSPR) Optical Fiber Sensor for Sensitive Detection of Mercury(II) Ion by Gold Nanoparticles-DNA Conjugates. *Biosens. Bioelectron.* **2018**, *114*, 15−21.

(25) Wan, M.; Luo, P.; Jin, J.; Xing, J.; Wang, Z.; Wong, S. T. C. Fabrication of Localized Surface Plasmon Resonance Fiber Probes Using Ionic Self-assembled Gold Nanoparticles. *Sensors* **2010**, *10*, 6477−6487.

https://dx.doi.org/10.1021/acsami.0c09711
ACS Appl. Mater. Interfaces XXXX, XXX, XXX−XXX

(26) Kim, H. M.; Jin, S. M.; Lee, S. K.; Kim, M.-G.; Shin, Y.-B. Detection of Biomolecular Binding through Enhancement of Localized Surface Plasmon Resonance (LSPR) by Gold Nanoparticles. *Sensors* **2009**, *9*, 2334−2344.
(27) Oldenburg, S. J.; Averitt, R. D.; Westcott, S. L.; Halas, N. J. Nanoengineering of Optical Resonances. *Chem. Phys. Lett.* **1998**, *288*, 243−247.
(28) Liang, G.; Zhao, Z.; Wei, Y.; Liu, K.; Hou, W.; Duan, Y. Plasma Enhanced Label-Free Immunoassay for Alpha-Fetoprotein Based on A U-bend Fiber-optic LSPR Biosensor. *RSC Adv.* **2015**, *5*, 23990−23998.
(29) Yockell-Lelièvre, H.; Lussier, F.; Masson, J.-F. Influence of the Particle Shape and Density of Self-Assembled Gold Nanoparticle Sensors on LSPR and SERS. *J. Phys. Chem. C* **2015**, *119*, 28577−28585.
(30) Chauhan, S. K.; Punjabi, N.; Sharma, D. K.; Mukherji, S. A Silicon Nitride Coated LSPR Based Fiber-Optic Probe for Possible Continuous Monitoring of Sucrose Content in Fruit Juices. *Sens. Actuators, B* **2016**, *222*, 1240−1250.
(31) Bastús, N. G.; Comenge, J.; Puntes, V. Kinetically Controlled Seeded Growth Synthesis of Citrate-Stabilized Gold Nanoparticles of Up to 200 nm: Size Focusing Versus Ostwald Ripening. *Langmuir* **2011**, *27*, 11098−11105.
(32) Willets, K. A.; Van Duyne, R. P. Localized Surface Plasmon Resonance Spectroscopy and Sensing. *Annu. Rev. Phys. Chem.* **2007**, *58*, 267−297.
(33) Mayer, K. M.; Lee, S.; Liao, H.; Rostro, B. C.; Fuentes, A.; Scully, P. T.; Nehl, C. L.; Hafner, J. H. A Label-Free Immunoassay Based Upon Localized Surface Plasmon Resonance of Gold Nanorods. *ACS Nano* **2008**, *2*, 687−692.
(34) Zhang, Z.; Wang, H.; Chen, Z.; Wang, X.; Choo, J.; Chen, L. Plasmonic Colorimetric Sensors Based on Etching and Growth of Noble Metal Nanoparticles: Strategies and Applications. *Biosens. Bioelectron.* **2018**, *114*, 52−65.
(35) Wei, A.; Leonov, A. P.; Wei, Q. *Gold Nanorods: Multifunctional Agents for Cancer Imaging and Therapy*; Humana Press, 2010; Vol. *1*; pp 119−130.
(36) Dreaden, E. C.; Alkilany, A. M.; Huang, X.; Murphy, C. J.; El-Sayed, M. A. The Golden Age: Gold Nanoparticles for Biomedicine. *Chem. Soc. Rev.* **2012**, *41*, 2740−2779.
(37) Huang, X.; Neretina, S.; El-Sayed, M. A. Gold Nanorods: From Synthesis and Properties to Biological and Biomedical Applications. *Adv. Mater.* **2009**, *21*, 4880−4910.
(38) Vigderman, L.; Khanal, B. P.; Zubarev, E. R. Functional Gold Nanorods: Synthesis, Self-Assembly, and Sensing Applications. *Adv. Mater.* **2012**, *24*, 4811−4841.
(39) Huff, T. B.; Hansen, M. N.; Zhao, Y.; Cheng, J.-X.; Wei, A. Controlling The Cellular Uptake of Gold Nanorods. *Langmuir* **2007**, *23*, 1596−1599.
(40) Alkilany, A. M.; Nagaria, P. K.; Hexel, C. R.; Shaw, T. J.; Murphy, C. J.; Wyatt, M. D. Cellular Uptake and Cytotoxicity of Gold Nanorods: Molecular Origin of Cytotoxicity and Surface Effects. *Small* **2010**, *5*, 701−708.
(41) Manoharan, H.; Kc, D.; Sai, V. V. R. Controlled In Situ Seed-Mediated Growth of Gold and Silver Nanoparticles on An Optical Fiber Platform for Plasmonic Sensing Applications. *Plasmonics* **2020**, *15*, 51−60.
(42) Lee, B.; Park, J.-H.; Byun, J.-Y.; Kim, J. H.; Kim, M.-G. An Optical Fiber-Based LSPR Aptasensor for Simple and Rapid In-Situ Detection of Ochratoxin A. *Biosens. Bioelectron.* **2018**, *102*, 504−509.
(43) Schulz, F.; Friedrich, W.; Hoppe, K.; Vossmeyer, T.; Weller, H.; Lange, H. Effective PEGylation of Gold Nanorods. *Nanoscale* **2016**, *8*, 7296−7308.
(44) Luan, J.; Naik, R. R.; Singamaneni, S.; Morrissey, J. J.; Wang, Z.; Derami, H. G.; Liu, K. K.; Cao, S.; Jiang, Q.; Wang, C. Add-On Plasmonic Patch as A Universal Fluorescence Enhancer. *Light: Sci. Appl.* **2018**, *7*, 29.
(45) Urrutia, A.; Goicoechea, J.; Rivero, P. J.; Pildain, A.; Arregui, F. J. Optical Fiber Sensors Based on Gold Nanorods Embedded in Polymeric Thin Films. *Sens. Actuators, B* **2017**, *255*, 2105−2112.
(46) Feng, A. L.; You, M. L.; Tian, L.; Singamaneni, S.; Liu, M.; Duan, Z.; Lu, T. J.; Xu, F.; Lin, M. Distance-dependent Plasmon-Enhanced Fluorescence of Upconversion Nanoparticles Using Polyelectrolyte Multilayers as Tunable Spacers. *Sci. Rep.* **2015**, *5*, 7779.
(47) Daniel, M.-C.; Astruc, D. Gold Nanoparticles: Assembly, Supramolecular Chemistry, Quantum-Size-Related Properties, and Applications Toward Biology, Catalysis, and Nanotechnology. *Chem. Rev.* **2004**, *104*, 293−346.
(48) Mao, M.; Zhou, B.; Tang, X.; Chen, C.; Ge, M.; Li, P.; Huang, X.; Yang, L.; Liu, J. Natural Deposition Strategy for Interfacial, Self-assembled, Large-Scale, Densely Packed, Monolayer Film with Ligand-Exchanged Gold Nanorods for In Situ Surface-enhanced Raman Scattering Drug Detection. *Chem.—Eur. J.* **2018**, *24*, 4094−4102.
(49) Lopes, W. A.; Jaeger, H. M. Hierarchical Self-Assembly of Metal Nanostructures on Diblock Copolymer Scaffolds. *Nature* **2001**, *414*, 735−738.
(50) Park, S.; Kim, B.; Wang, J.-Y.; Russell, T. P. Fabrication of Highly Ordered Silicon Oxide Dots and Stripes from Block Copolymer Thin Films. *Adv. Mater.* **2008**, *20*, 681−685.
(51) Zhu, H.; Masson, J.-F.; Bazuin, C. G. Monolayer Arrays of Nanoparticles on Block Copolymer Brush Films. *Langmuir* **2019**, *35*, 5114−5124.
(52) Wang, C.; Mao, Y.; Wang, D.; Qu, Q.; Yang, G.; Hu, X. Fabrication of Highly Ordered Microporous Thin Films by PS-b-PAA Self-Assembly and Investigation of Their Tunable Surface Properties. *J. Mater. Chem.* **2008**, *18*, 683.
(53) Ludwigs, S.; Schmidt, K.; Krausch, G. One-dimensional Swelling of A pH-Dependent Nanostructure Based on ABC Triblock Tterpolymers. *Macromolecules* **2005**, *38*, 2376−2382.
(54) Ye, X.; Zheng, C.; Chen, J.; Gao, Y.; Murray, C. B. Using Binary Surfactant Mixtures to Simultaneously Improve The Dimensional Tunability and Monodispersity in the Seeded Growth of Gold Nanorods. *Nano Lett.* **2013**, *13*, 765−771.
(55) Ye, X.; Jin, L.; Caglayan, H.; Chen, J.; Xing, G.; Zheng, C.; Doan-Nguyen, V.; Kang, Y.; Engheta, N.; Kagan, C. R.; König, C. B. Improved Size-Tunable Synthesis of Monodisperse Gold Nanorods through the Use of Aromatic Additives. *ACS Nano* **2012**, *6*, 2804−2817.
(56) KNig, T. A.; Ledin, P. A.; Kerszulis, J.; Mahmoud, M. A.; El-Sayed, M. A.; Reynolds, J. R.; Tsukruk, V. V. Electrically Tunable Plasmonic Behavior of Nanocube−Polymer Nanomaterials Induced by A Redox-Sctive Electrochromic Polymer. *ACS Nano* **2014**, *8*, 6182−6192.
(57) Wang, Q.; Jing, J. Y.; Wang, B. T. Highly Sensitive SPR Biosensor Based on Graphene Oxide and Staphylococcal Protein A Co-Modified TFBG for Human IgG Detection. *IEEE Trans. Instrum. Meas.* **2018**, *68*, 3350−3357.
(58) Wong, W. C.; Chan, C. C.; Boo, J. L.; Teo, Z. Y.; Tou, Z. Q.; Yang, H. B.; Li, C. M.; Leong, K. C. Photonic Crystal Fiber Surface Plasmon Resonance Biosensor Based on Protein G Immobilization. *IEEE J. Sel. Top. Quantum Electron.* **2013**, *19*, 4602107.
(59) Socorro, A. B.; Corres, J. M.; Del Villar, I.; Arregui, F. J.; Matias, I. R. Fiber-Optic Biosensor Based on Lossy Mode Resonances. *Sens. Actuators, B* **2012**, *174*, 263−269.
(60) Cao, J.; Sun, T.; Grattan, K. T. V. Development of Gold Nanorod-Based Localized Surface Plasmon Resonance Optical Fiber Biosensor. *Int. Soc. Opt. Eng.* **2012**, *181*, 611−619.

https://dx.doi.org/10.1021/acsami.0c09711
ACS Appl. Mater. Interfaces XXXX, XXX, XXX−XXX